Numerical Heat Transfer, Part A: Applications: An International Journal of Computation and Methodology
Publication details, including instructions for authors and subscription information:
http://www.tandfonline.com/loi/unht20

Performance Simulation and Thermal Stress Analysis of Ceramic Recuperators formed by SiC and MAS

Chun-Hsiang Yang [a] , Ming-Ta Yu [a] , Chiun-Heng Chen [a] & Chiun-Hsun Chen [a]

[a] Department of Mechanical Engineering , National Chiao Tung University , Hsinchu, Taiwan, Republic of China

Published online: 14 Dec 2007.

To cite this article: Chun-Hsiang Yang , Ming-Ta Yu , Chiun-Heng Chen & Chiun-Hsun Chen (2007) Performance Simulation and Thermal Stress Analysis of Ceramic Recuperators formed by SiC and MAS, Numerical Heat Transfer, Part A: Applications: An International Journal of Computation and Methodology, 53:7, 709-725, DOI: 10.1080/10407780701715794

To link to this article: http://dx.doi.org/10.1080/10407780701715794

Numerical Heat Transfer, Part A, 53: 709–725, 2008

ISSN: 1040-7782 print/1521-0634 online
DOI: 10.1080/10407780701715794

Taylor & Francis
Taylor & Francis Group

PERFORMANCE SIMULATION AND THERMAL STRESS ANALYSIS OF CERAMIC RECUPERATORS FORMED BY SIC AND MAS

Chun-Hsiang Yang, Ming-Ta Yu, Chiun-Heng Chen, and Chiun-Hsun Chen

Department of Mechanical Engineering, National Chiao Tung University, Hsinchu, Taiwan, Republic of China

This study conducted performance simulations for ceramic recuperators and performed thermal stress analysis to provide reliable guidance for heat recuperator designers. A numerical simulation was conducted utilizing STAR-CD to predict thermal and pressure flow fields inside two 50 W ceramic compact heat exchangers, one made of SiC and the other made of MAS. The predicted temperature and pressure profiles from performance simulations were then used to compute thermal stress analysis of the ceramic plate recuperators. Thus, three issues were discussed—the impact of fluid pressure and the thermal expansion on the ceramic recuperators, the effects of the constraint condition of the model boundary on the ceramic plates, and the different effects of the two different ceramic recuperator cores could made to the outer metal shells.

1. INTRODUCTION

More than 60% of the total energy input to high-temperature furnaces is wasted in the stack when no energy saving/recovering facility exists. To conserve energy, designing a recuperative waste heat-recovery system is crucial to reducing the amount of energy lost in furnace exhaust gases, which are typically about 1000–1300°C. Therefore, designing a high-temperature-resistant heat exchanger capable of operating in such an environment is necessary.

Dziedzic et al. [1] presented their design of ceramic compact heat exchanger in United Status Patent, which consists of a ceramic crossflow recuperator core, a metallic housing around the core, and the gaskets between ceramics and metal. The thermal insulation between core, and housing minimized heat loss through the metallic housing. The gaskets could prevent leakage produced by the different thermal expansions between ceramics and metal. Jeffrey et al. [2] developed various types of ceramic compact heat exchangers named super recupers. Young et al. [3] also developed ceramic finned-plate recuperator named CERHX. Both ceramic recuperators are now on the market. Kleiner et al. [4] showed that, comparing to general metal heat exchanger, the ceramic heat exchanger has higher temperature

Received 21 May 2007; accepted 10 September 2007.

Address correspondence to Chiun-Hsun Chen, Department of Mechanical Engineering, National Chiao-Tung University, HsinChu, Taiwan 30050, R.O.C. E-mail: chchen@mail.nctu.edu.tw

NOMENCLATURE

A	surface area	U	overall heat-transfer coefficient
C	empirical coefficients	u	velocity, m/s
E	empirical coefficients	u^+	velocity scale value
F_h	diffusional thermal energy flux, W/m^2	x_i	Certesian coordinate
g	gravity, m/s^2	y^+	length scale value
H	enthalpy, KJ/Kg	ΔX	wall thickness
K	flow coefficient	δ_{ij}	Kronecker Delta
k	thermal conductivity, W/mK	ρ	density, kg/m^3
P	pressure, N/m^2	ε	turbulence dissipation
Q	the volumetric flow rate	κ	empirical coefficients
Re	Reynolds number	μ	viscosity, kg/ms
s_{ij}	the rate of strain tensor	σ	empirical coefficients
s_h	energy source	τ	shear stress
T	temperature, K	τ_{ij}	stress tensor component

capabilities without the need of extra equipment to control temperature. This research also reduced the stresses and increased product durability by changing the geometry of ceramic matrices. Coombs et al. [5] presented a ceramic recuperator, which contained a cast-ceramic finned plate. The proposed recupeator had the capability of operating in the flue gas temperature up to 1350°C to provide 1100°C preheated combustion air. The recuperator could also save in excess of 50% fuel consumption while being used in an unrecupterated furnace. Mario [6] had found an advanced ceramic material and named it "Hexalloy SA silicon Carbide," whose high heat conductivity was suitable for recuperators. Ward et al. [7] carried out a series of anti-corrosion experiments to test the alpha-sintered SiC and Coors reaction bonded SiC tubes in a recuperator. The heat exchanger was installed in an aluminum reverberatory remelt furnace which required salt-based chlorine fluxing agents to operate. Experiment results showed no visible signs of corrosion on both tested materials. Ranganayakulu et al. [8, 9] investigated the combined effects of longitudinal heat conduction, inlet flow nonuniformity, and temperature nonuniformity on thermal performance in cross-flow plate heat exchanger. The investigations found that, under large NTU (number of transfer unit), the deterioration of exchanger performance caused by nonuniform flow on both flow sides are very limited. While designing a heat exchanger, the analysis of minimum entropy generation number of Ogulata's et al. [10] was based on the second law of thermodynamics in the cross-flow heat exchanger. The effects of optimum flow path length and dimensionless mass velocity on minimum entropy generation number were also analyzed theoretically and experimentally. Bourisa et al. [11] tried to modify a tube bundle heat exchanger to achieve a higher heat transfer capability. The optimized shape of tube among three different cross sections was determined after the efficiency of corresponding recuperators was compared and simulated. Shojaefard et al. [12] tried to model the transient thermal analysis of an exhaust valve with finite-element method. The temperature distribution and resultant thermal stress were obtained by ANSYS. Demirdzic et al. [13] proposed a novel finite-volume method, adopting temperature-time equivalence hypothesis to solve the linear thermoviscoelastic deformation

problem. Tsuzuki et al. [14] had done the three dimension thermal-hydraulic simulation of printed circuit heat exchanger by applying the computer code, FLUENT. The optimized flow channel design was accomplished by changing the fin shape and angle to reduce pressure drop and increase heat transfer performance.

This study first applied Star-CD, to simulate real operational conditions of a ceramic recuperator. If maximal thermal stress in the ceramic recuperator exceeded a critical value, the design was ineffective and should be modified accordingly. The thermal-flow and subsequent thermal stress simulations were then performed again to confirm the effectiveness of the readjustment. The procedure continues until modifications met design criteria. Thus, optimal design of a ceramic heat exchanger with high thermal efficiency and low thermal stress was achieved. Following performance simulations for the ceramic recuperator, the generated temperature, velocity, and

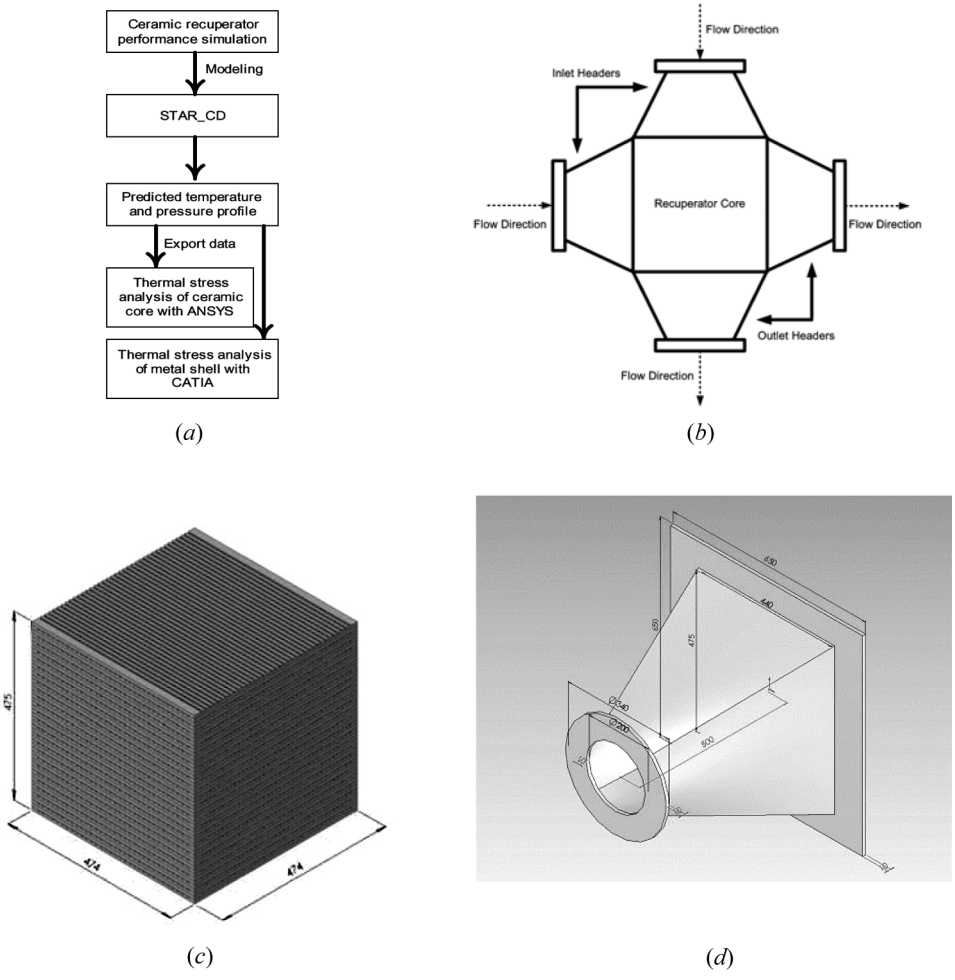

Figure 1. (*a*) Simulation flow chart; (*b*) heat exchanger configuration scheme; (*c*) geometric design of the ceramic core; and (*d*) geometric design of the header.

pressure distributions were used as input data for the subsequent simulations of thermal stress distributions that employed ANSYS in a ceramic plate and CATIA in the metal shell. Figure 1*a* presented the simulation flow chart.

2. PHYSICAL SYSTEM

Figure 1*b* presented the configuration of the core and headers. The numerical simulation model for the ceramic plate recuperator included a ceramic core and headers around the core. Flue gas and preheated air flowed into the heat exchanger from inlet headers, exchanged heat via thermal conduction of the ceramic plate when passing through individual passages, and finally flowed out of the heat exchanger via the outlet headers. The ceramic materials used in the heat exchanger designed by the Industrial Technology Research Institute (ITRI) were SiC and MAS. The highest temperature of exhaust gases was 1000°C (1273 K), and the lowest temperature of preheated air was 27°C (300 K).

3. MATHEMATICAL MODEL

3.1. Basic Assumptions

In the first step, simulations were performed for the three-dimensional, steady thermo-flow field inside the ceramic recuperator, which comprised an array of cast ceramic plates. The flue gas and preheated air passed through their individual passages and exchanged heat via the thermal conduction of ceramic plates. The areas of simulation were ceramic cores, and inlet and outlet headers. The following assumptions were made to increase the tractability of the problem: the flow was Newtonian fluid; the flow was steady, compressible, and turbulent; flue gases were hot air and gaseous behaviors obeyed the ideal gas law. Although the thermal conductivity of solid might be temperature dependency [15], it was rather difficult to cite previous researches for these parameters which would be changed with different forming process and structure. The thermal conductivities of SiC and MAS in this research were assumed constant, which was measured by the HotDisk thermal constant analyzer at room temperature.

3.2. Governing Equation

The flow was assumed as a three-dimensional, turbulent flow. The $k-\varepsilon$ model, SIMPLE algorithm and hybrid scheme were utilized to solve these problems [16]. The major governing equations were as follows.

Continuity equation

$$\frac{\partial \rho}{\partial t} + s\frac{\partial}{\partial x_j}(\rho u_j) = 0 \tag{1}$$

Momentum equation

$$\frac{\partial \rho u_i}{\partial t} + \frac{\partial}{\partial x_j}(\rho u_j u_i - \tau_{ij}) = -\frac{\partial p}{\partial x_i} \tag{2}$$

where suffixes i and j represent Certesian coordinates ($i = 1, 2, 3$), u_i and u_j are absolute fluid-velocity components in directions of x_i and x_j, respectively, ρ is density, t is time, τ_{ij} is the stress tensor component, and p is pressure.

For turbulent flow, u_i, p and other dependent variables, including τ_{ij}, assume their ensemble averaged values. For a Newtonian fluid, 32

$$\tau_{ij} = 2\mu s_{ij} - \frac{2}{3}\mu \frac{\partial u_k}{\partial x_k}\delta_{ij} - \overline{\rho u_i' u_j'} \tag{3}$$

$$s_{ij} = \frac{1}{2}\left(\frac{\partial u_i}{\partial x_j} + \frac{\partial u_j}{\partial x_i}\right) \tag{4}$$

where μ is the molecular dynamic fluid viscosity; δ_{ij} is the Kronecker delta, which is unity when $i = j$ and zero otherwise; s_{ij} is the rate of strain tensor; u' is fluctuation of the ensemble average velocity; and the overbar denotes the ensemble averaging process.

Total enthalpy equation

$$\frac{\partial(\rho H)}{\partial t} + \frac{\partial}{\partial x_i}(\rho \overline{u_j} H - F_{h,j} - u_i \tau_{ij}) = \frac{\partial P}{\partial t} - \frac{\partial}{\partial x_j}(u_{cj} p) + s_i u_i + s_h \tag{5}$$

where $F_{h,j}$ is diffusional thermal energy flux in direction x_j, and s_h is the energy source.

Turbulent model. Generally, the instant property for turbulent flow was the sum of the mean value and the fluctuation. The Navier-Stokes equation was used, which leads to the Reynolds averaged equation.

$$\rho \overline{u_j}\frac{\partial \overline{u_i}}{\partial x_j} = \rho \overline{f_i} - \frac{\partial \overline{p}}{\partial x_i} + \frac{\partial}{\partial x_j}\left(\mu \frac{\partial \overline{u_i}}{\partial x_j} - \rho \overline{u_i' u_j'}\right) \tag{6}$$

There are ten unknowns in this equation (mean pressure, mean velocities in three directions and six Reynolds stresses, $-\rho\overline{u_i' u_j'}$); however, only four equations exist. This study used $k - \varepsilon$ turbulent models for governing system closure. The Reynolds stress equation was

$$-\rho \overline{u_i' u_j'} = \mu_t\left(\frac{\partial u_i}{\partial x_j} + \frac{\partial u_j}{\partial x_i}\right) - \frac{2}{3}\left(\mu_t \frac{\partial u_k}{\partial x_k} + \rho k\right)\delta_{ij} \tag{7}$$

wherein μ_t is turbulent viscosity and k is turbulent kinetic energy; in addition, $k = \frac{\overline{u_i' u_j'}}{2}$ and $\mu_t = f_\mu \frac{c_\mu \rho k^2}{\varepsilon}$, in which c_μ and f_μ are experience coefficients with the values of 0.09

and 1, respectively. Via the turbulent model, the turbulence energy equation is

$$\frac{\partial}{\partial x_j}\left(\rho u_j k - \frac{\mu_{\text{eff}}}{\sigma_k}\frac{\partial k}{\partial x_j}\right) = \mu_t(p - p_B) - \rho\varepsilon - \frac{2}{3}\left(\mu_t\frac{\partial u_i}{\partial x_i} + \rho k\right)\frac{\partial u_i}{\partial x_i} \tag{8}$$

Turbulence dissipation rate equation

$$\frac{\partial}{\partial x_j}\left[\rho\overline{u_j}\varepsilon - \frac{\mu_{\text{eff}}}{\sigma_\varepsilon}\frac{\partial \varepsilon}{\partial x_j}\right] = C_{\varepsilon 1}\frac{\varepsilon}{k}\left[\mu_t P - \frac{2}{3}\left(\mu_t\frac{\partial u_i}{\partial x_i} + \rho k\right)\frac{\partial u_i}{\partial x_i}\right] + C_{\varepsilon 3}\frac{\varepsilon}{K}\mu_t P_B - C_{\varepsilon 2}\rho\frac{\varepsilon^2}{K} + C_{\varepsilon 4}\rho\varepsilon\frac{\partial u_i}{\partial x_i} \tag{9}$$

wherein $\mu_{\text{eff}} = \mu + \mu_t$, $P = 2s_{ij}\frac{\partial u_i}{\partial x_j}$ and $P_B = -\frac{g_i}{\sigma_{h,t}}\frac{1}{\rho}\frac{\partial \rho}{\partial x_i}$. In addition, $C_{\varepsilon 1} = 1.44$, and $C_{\varepsilon 2} = 1.92$, $C_{\varepsilon 3} = 1.44$ for $P_B > 0$, otherwise $= 0$ and $C_{\varepsilon 4} = -0.33$ and these parameters are empirical coefficients.

3.3. Wall Functions

The main assumptions on which the wall functions employed were based were as follows: variations in velocity were normal to the wall, leading to one-dimensional behavior; effects of pressure gradients and body force were negligible; shear stress and velocity vectors were aligned and unidirectional throughout the layer; and a balance exists between turbulence energy production and dissipation.

The resulting formulae giving the cross stream profiles in terms of the normal distance y from the wall were

$$u^+ = \begin{cases} y^+ & y^+ \le y_m^+ \\ \frac{1}{k}\ln(Ey^+) & y^+ > y_m^+ \end{cases} \tag{10}$$

wherein $u^+ = \frac{(u-u_w)}{\sqrt{(\tau_w/\rho)}}$, $y^+ = \frac{\rho C_v^{1/4}k^{1/2}y}{\mu}$, and y_m^+ satisfies the equation $y_m^+ - \frac{1}{k}\ln(Ey_m^+) = 0$, in which u_w is wall velocity, τ_w is wall shear stress, and k and E are empirical coefficients.

3.4. Boundary Conditions

3.4.1. Ceramic recuperator. To save calculation time and to compromise the memory limit of computer, this study separated the ceramic recuperator into the following five parts: ceramic core; flue gas inlet header; flue gas outlet header; preheated air inlet header; and preheated air outlet header. Each part was calculated individually.

3.4.2. The inlet boundary conditions. The headers had only one inlet, whereas the recuperator core had two inlets. The flow rates and temperatures of flue gas and preheated air at header inlets were defined by ITRI. Conversely, other inlet conditions were calculated based on temperature, flow rate, and empirical formula. The fluids in both inlet headers were air. The other inlet conditions of inlet headers were listed in Table 1.

Table 1. Inlet conditions of inlet headers

	Flue gas	Preheated air
Temperature	1273 K	300 K
Flow rate	~5NCMM	~5NCMM
Velocity	11.33 m/s (uniform flow)	2.67 m/s (uniform flow)
Density ρ (T)	$0.277\,kg/m^3$	$1.194\,kg/m^3$
Viscosity μ (T)	$47.9 \times 10^{-6}\,Pa \cdot s$	$18.4 \times 10^{-6}\,Pa \cdot s$
Reynolds number	Re = 13104	Re = 34,360
Turbulence length scale	0.2	0.05
Turbulence intensity	0.2	0.05

3.4.3. The outlet boundary conditions. The outlet conditions of heaters and the recuperator core in the STAR-CD were set to the outlet boundary. These conditions were unknown, mainly determined by what was occurring upstream. Pressure at the outlet boundary was defined as zero. Temperature, velocity, and pressure at the outlet boundary were assumed to have zero gradients, and the flow rate at the in outlet boundary must satisfy mass balance.

3.4.4. Wall boundary conditions. Except at the inlet and outlet boundaries, the whole geometry was all wall boundaries, which were the no-slip boundary conditions ($u, v, w = 0$) for velocity and adiabatic for temperature.

4. NUMERICAL METHOD

To solve the incompressible Navier-Stokes equation, the SIMPLE algorithm, which is a widely used numerical method, was applied. This algorithm adopts the finite volume method and, different from other algorithms, also adopts the finite difference method. Figure 1*c* presented the model of the heat exchanger core. The heat exchanger model has 2,200,000 cells and 780,000 couples. The SiC material can be changed to MAS by changing the solid properties in the heat exchanger model. Figure 1*d* presented the geometrical design of header. The header has 28,468 cells and 528 couples. With low cost and high performance personal computer (PC) systems and high-speed networks, a PC Cluster is a cost-effective alternative for parallel/distributed computing solution.

5. PERFORMANCE SIMULATION RESULT

5.1. Inlet Header

Figures 2*a*–2*d* presented the performance simulation results for the inlet heater. Figures 2*a* and 2*b* presented the velocity distributions in both inlet headers. The flow speed decreases and pressure increases due to the area change to the cross section. Because of the wall friction, the momentum of the fluid layer near the surface was not high enough to overcome adverse pressure gradient. As the velocity gradient at the surface becomes zero, the flow has reached a separation point, behind which

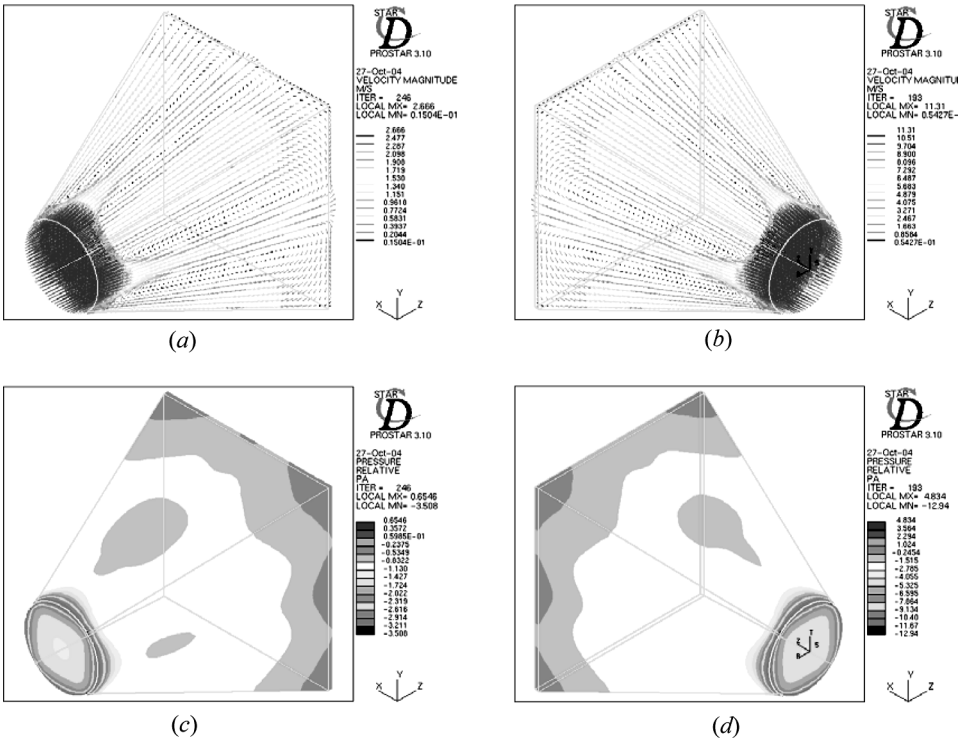

Figure 2. Simulated performance of the inlet header. (*a*) Velocity distribution of preheated air; (*b*) velocity distribution of flue gas; (*c*) pressure distribution of preheated air; and (*d*) pressure distribution of flue gas.

a reverse flow occurs. Figures 2*c* and 2*d* presented the corresponding pressure distributions. The inlet pressure was lower than that at the outlet. The reason for this relationship is the same as that mentioned above.

5.2. Recuperator Core

Figures 3*a* and 3*b* showed the temperature distributions of the SiC and MAS recuperator cores, whose properties were listed in Table 2. The irregular distribution atop the core structure was affected by the passage. Because the mesh resolution was not sufficiently high in the passage and local flow velocity was high, a jump existed between the solid and adjacent fluid layer temperatures. Since the thermal conductivity of SiC which was high, the corresponding temperature jump was not as obvious as that for MAS. Around the corner located between two outlets of flue gas and preheated air, the outlet temperature of preheated air was higher than that of flue gas; consequently, a reverse temperature profile occurs (Figures 3*a* and 3*b*).

Figures 4*a*–4*d* presented the pressure distributions in SiC and MAS recuperators. These data were all gauged pressure. Due to the reduction in cross-sectional area at the interface between the inlet header and passage, a dynamic loss occurred and pressure dropped immediately. When the fluid passed through the passage,

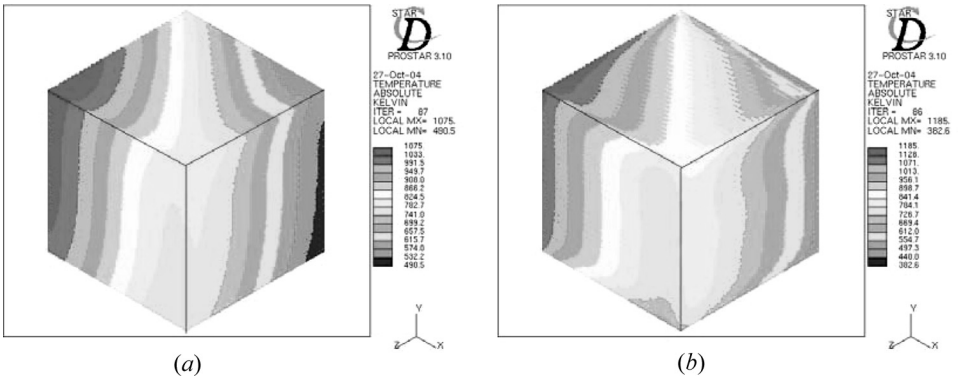

(*a*) (*b*)

Figure 3. (*a*) Temperature distributions of the SiC recuperator core and (*b*) temperature distributions of the MAS recuperator core.

pressure decreased due to a friction effect. At the core passage outlet, pressure increased as the cross-sectional area increases. At the recuperator core outlet, the flow speed decreased further due to the increased cross-sectional area of outlet header.

Figures 5*a* and 5*b* presented the heat transfer coefficient (H-coefficient) distributions for the SiC and MAS recuperators, which were the directly output data from the simulation results of STAR-CD [17]. The *H*-coefficients were primarily utilized for calculating *U* (overall heat transfer coefficient).The parameter *U* was the primary parameter in the LMTD and the ε-NTU methods, which estimated the efficiency of the heat exchangers. *U* was defined by the following relation [18].

$$\frac{1}{U} = \frac{A}{h_1 A_{w1}} + \frac{\Delta X}{k} + \frac{A}{h_2 A_{w2}} \tag{11}$$

wherein k is thermal conductivity, A is the total surface area, A_{w1} is surface area in fluid 1, A_{w2} is surface area in fluid 2, h_1 is convection heat-transfer coefficient in fluid 1, h_2 is convection heat-transfer coefficient in fluid 2, and ΔX is wall thickness. The mean *H*-coefficients of the SiC recuperator in flue gas and preheated air obtained from STAR-CD simulations were 13.349 and 16.496 W/m^2k, respectively; the corresponding mean *H*-coefficients for the MAS recuperator were 13.749 and 17.429 W/m^2k, respectively.

The mean temperatures of the flue gas flow leaving the heat exchanger was 716.38 K for the SiC recuperator and 716.72 K for the MAS recuperator. The corresponding mean temperatures for the preheated air were 874.37 K and

Table 2. Material properties of SiC and MAS

Material	Young's Modulus	Poisson's ratio	Thermal expansion coefficient	Thermal conductivity
SiC	152 GPa	0.3	5.9 E-6	36.5 $W m^{-1} k^{-1}$
MAS	125 GPa	0.2	2.9 E-6	1.3 $W m^{-1} k^{-1}$

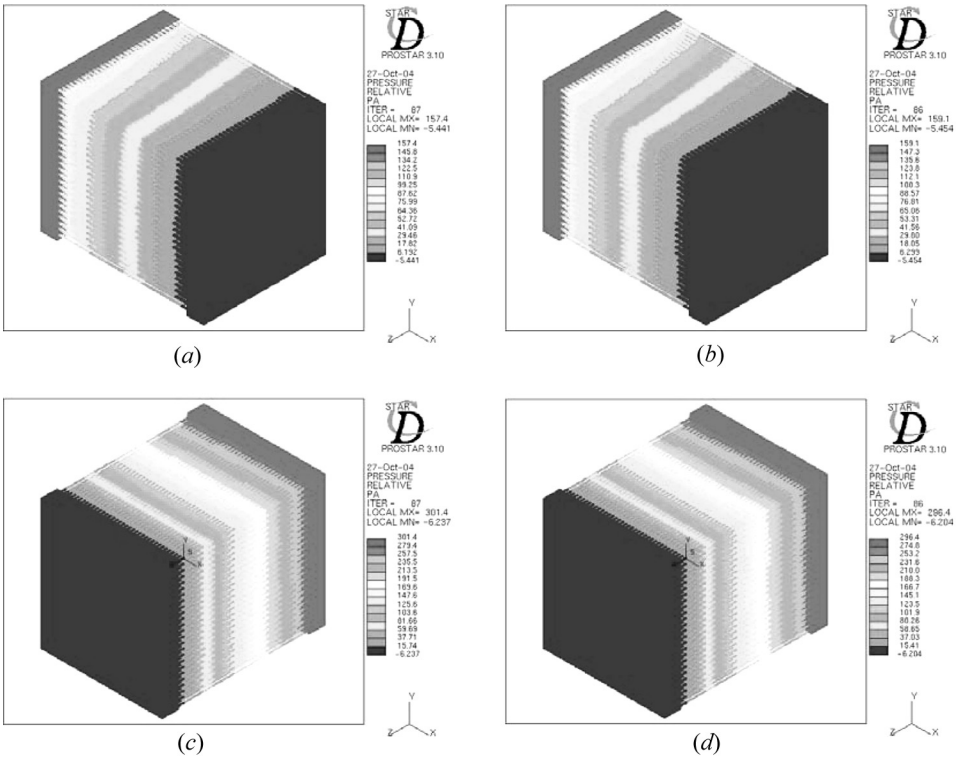

Figure 4. Pressure distributions of the recuperator core. (*a*) The SiC recuperator with flue gas; (*b*) the MAS recuperator with flue gas; (*c*) the SiC recuperator with preheated air; and (*d*) The MAS recuperator in preheated air.

878.13 K. The difference between inlet and outlet temperatures of the MAS recuperator was higher than that for the SiC recuperator. The following equation was then applied to calculate the heat transfer rate of the cross-flow heat exchanger

$$Q = UA\Delta T_m \tag{12}$$

where A is surface area of the heat transfer consistent with definition of U, and ΔT_m is the suitable mean temperature difference across the heat exchanger. As both recuperators have the same geometry, the surface areas of both recuperators were the same. The ΔT_m of the MAS recuperator was higher than that of the SiC recuperator. The thermal conductivity of the SiC recuperator was higher than that of MAS recuperator, implying that the U of SiC was greater than that of the MAS recuperator. Which recuperator had a higher total heat transfer rate could not be determined by Eq. (12) directly. The prediction from the STAR-CD simulation indicates that the SiC recuperator has a higher total heat transfer rate than the MAS recuperator.

Figures 6*a*–6*d* presented the heat flux distributions of the SiC and MAS recuperators. The heat flux in the top right corner, which was the intersection between

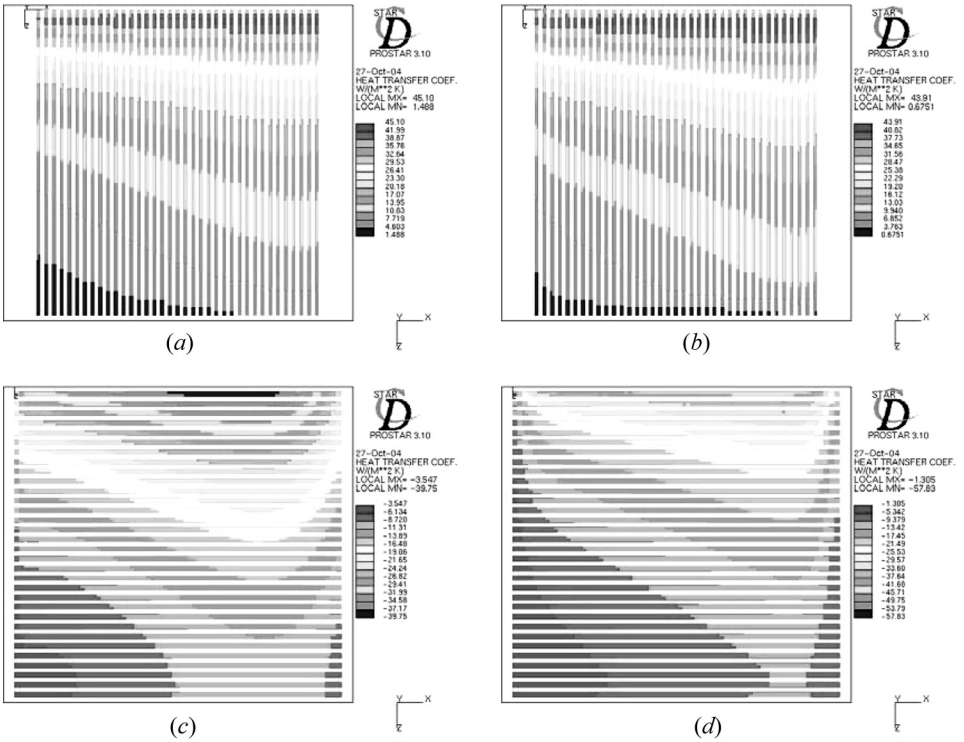

Figure 5. The *H*-coefficient distributions. (*a*) The SiC recuperator with preheated air; (*b*) the MAS recuperator with preheated air; (*c*) the SiC recuperator with flue gas; and (*d*) the MAS recuperator with flue gas.

inlets of flue gas and preheated air, was highest and reduced gradually as flue gas and preheated air moved outward. Mean heat flux of the SiC recuperator in flue gas was 6,234 W/m^2 and that for preheated air was 7,091 W/m^2. Mean heat flux of the MAS recuperator in flue gas was 6,232 W/m^2 and that for preheated air was 7,088 W/m^2. Mean heat flux multiplied by the heat-transfer surface area generated the total heat transfer rate. Total heat transfer rate for the SiC recuperator was 56.74 KW, and that for the MAS recuperator was 56.72 KW.

The analytical heat transfer rate of the SiC recuperator obtained using the above procedure was 59.12 KW, and that for the MAS recuperator was 57.98 KW. By installing an inlet header, the inlet flow through the ceramic core was nonuniform in real conditions. Thus, data predicted by STAR-CD differed from analytical data; the difference was roughly 2–4%, an insignificant difference.

5.3. Outlet Header

Figures 7*a*–7*d* presented the temperature distributions for outlet headers for both recuperators. As the flue gases exits the passages, they mixed with each other in the outlet header. The velocities of flue gas in the outlet headers were slower than those of preheated air; therefore, flue gas remains relatively longer in the header,

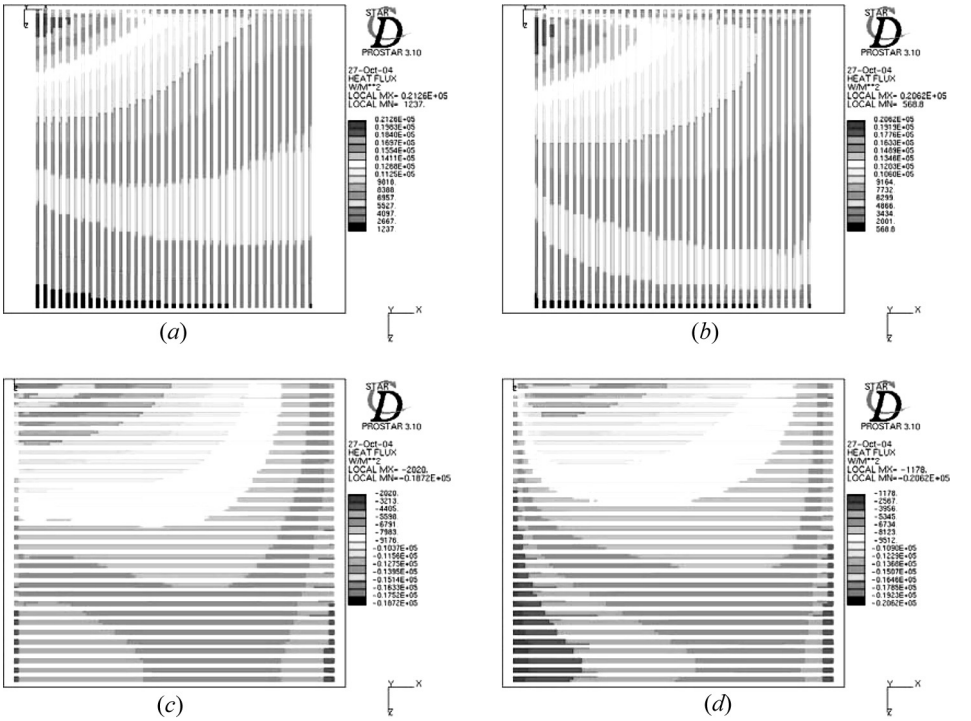

Figure 6. Heat flux distributions. (*a*) The SiC recuperator with preheated air; (*b*) the MAS recuperator with preheated air; (*c*) the SiC recuperator with flue gas; and (*d*) the MAS recuperator with flue gas.

thereby enhance the mixing and allowing the temperature to become relatively more uniform. Figures 7*e*–7*h* showed the pressure distributions in the outlet headers for both recuperators. The pressure decreased as velocity increased due to the decreased cross-sectional area. The lowest pressure occurred at the exit.

6. THERMAL STRESS ANALYSIS

Due to the importance of thermal stress analysis on brittle materials, the results and data generated by STAR-CD simulations were utilized during the second stage, thermal stress analysis, of the research. In this stage, ANSYS software was first applied for thermal stress analysis of the ceramic plate. The finite element method (FEM) results generated by STAR-CD simulations were directly imported into ANSYS software. Next, CATIA software was employed for thermal analysis of the metal shell—ANSYS software could not deal with nonlinear contact analysis between modeling parts. Since the recuperator core was fixed inside the metal shell, the constraint condition changed according to how the recuperator core was fixed. Therefore, after analyzing the effect of temperature and pressure fields using ANSYS, the constraint condition was analyzed and discussed. Recuperator core expansion caused by temperature and pressure fields triggered deformation of all modeling parts. The metal shell was the only part that did not release stress through deformation, as it

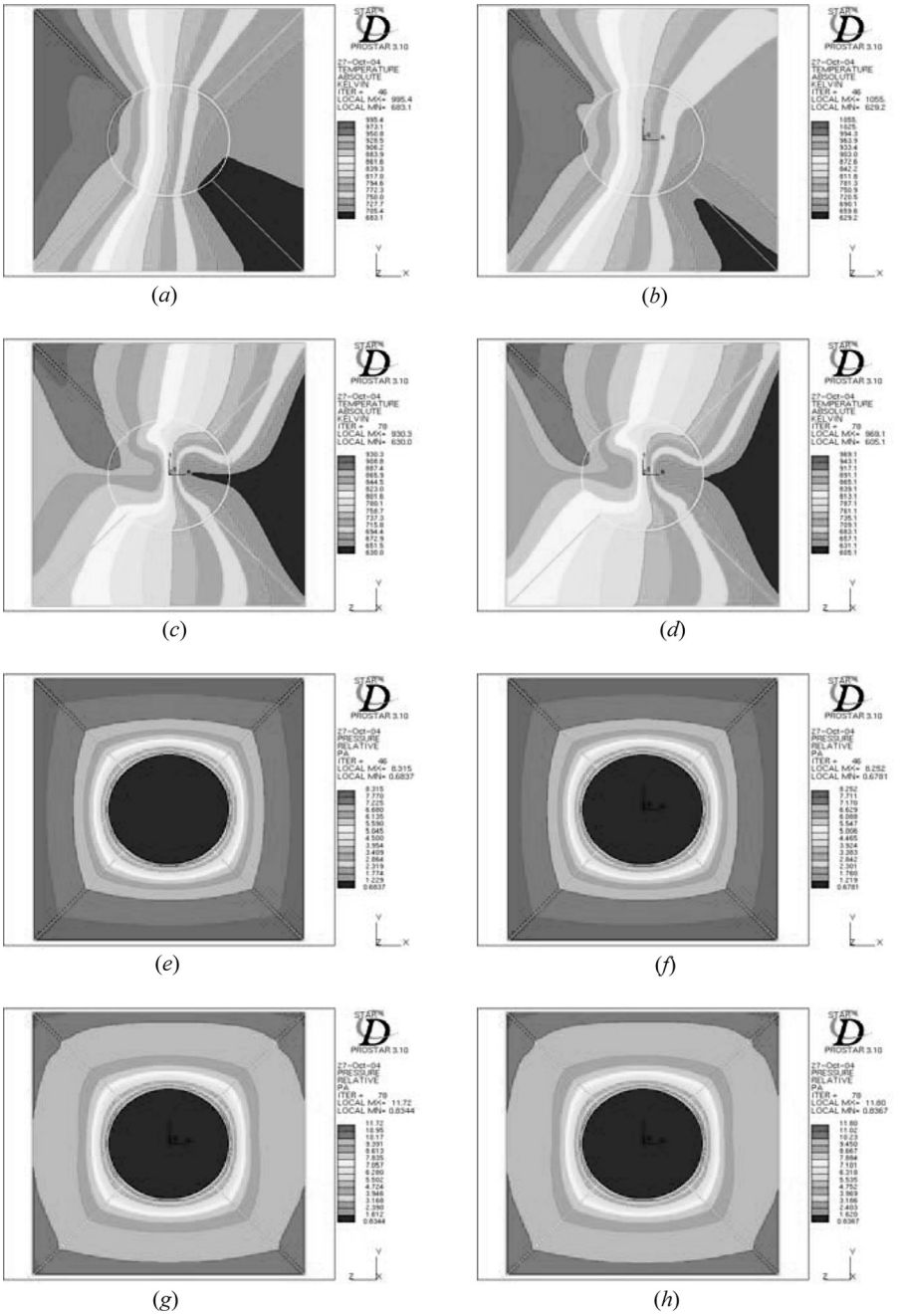

Figure 7. Simulation result of the outlet header. (*a*) Temperature distribution of the SiC recuperator with preheated air; (*b*) temperature distribution of the MAS recuperator with preheated air; (*c*) temperature distribution of the SiC recuperator with flue gas; (*d*) temperature distribution of the MAS recuperator with flue gas; (*e*) pressure distribution of the SiC recuperator with flue gas; (*f*) pressure distribution of the MAS recuperator with flue gas; (*g*) pressure distribution of the SiC recuperator with preheated air; and (*h*) pressure distribution of the MAS recuperator with preheated air.

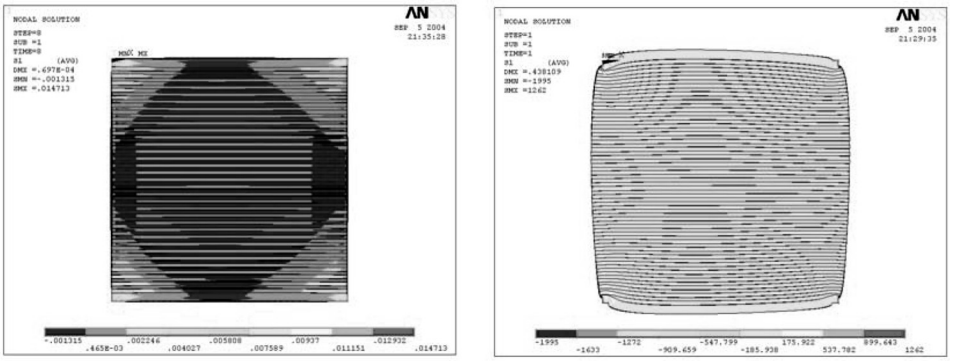

(*a*) (*b*)

Figure 8. Analytical results for thermal stress. (*a*) Stress when only applying a pressure field and (*b*) stress when only applying a temperature field.

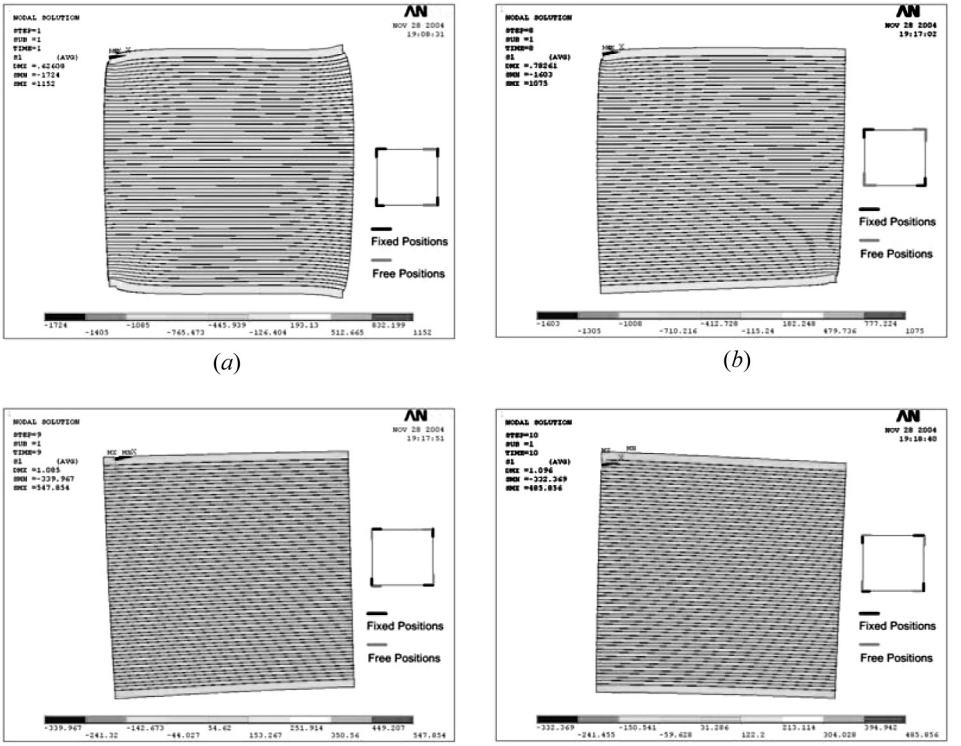

(*a*) (*b*)

(*c*) (*d*)

Figure 9. Thermal stress analysis under various constraint conditions. (*a*) First case of freeing two constraint positions; (*b*) second case of freeing four constraint positions; (*c*) third case of freeing four constraint positions; and (*d*) fourth case of freeing four constraint positions.

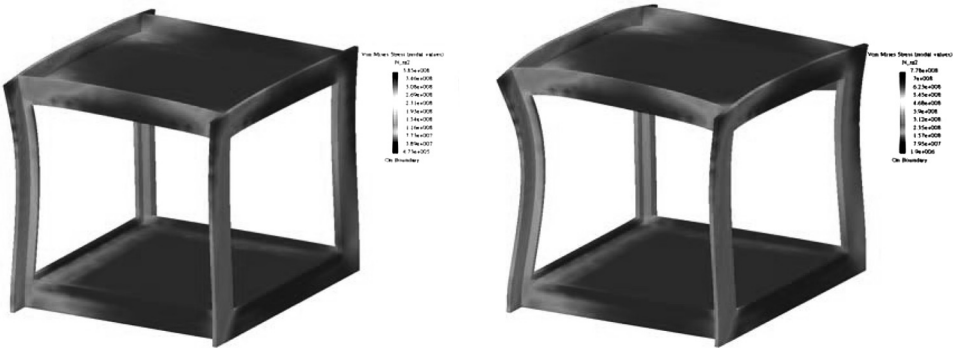

(*a*) (*b*)

Figure 10. The von Mises stress analytical result for the metal shell. (*a*) Ceramic recuperators made of MAS and (*b*) ceramic recuperators made of SiC.

closely wrapped around the recuperate core. Furthermore, due to the different ceramic materials SiC and MAS, the deformation of the metal shells differed. Consequently, CATIA was utilized to assess the effect analysis of von Mises stress, and determine the impacts of different ceramic materials on metal shell deformation.

7. RESULTS

Figure 8*a* showed the stress analysis result when only pressure field was applied to ceramic plates and Figure 8*b* showed the result that only temperature field was applied to ceramic plates. The effect of the temperature field was much greater than that of the pressure field. From direct observation, there were eight fixed positions. Figures 9*a*–9*d* presented the results of thermal stress analysis under different constraint conditions. The analysis here was only to compare the four subfigures 9*a*–9*d* each other that was a qualitative analysis. Figure 9*d* presented the most appropriate choices for fixed positions. Compared to all eight fixed positions, the thermal stress in Figure 9*d* was reduced by 50%. Figure 10*a* showed the von Mises stress for the metal shell when MAS was used to make the ceramic plate. Figure 10*b* showed the von Mises stress of the metal shell when SiC was used to make the ceramic plate. Because SiC had a larger thermal expansion coefficient than MAS, the thermal stress was greatest when SiC was used to make the ceramic plate.

8. CONCLUSIONS

This study utilized a commercial code, STAR-CD, to simulate heat transfer characteristics for two ceramic plate recuperators, a SiC recuperator and a MAS recuperator. Additionally, a parallel computing algorithm was employed to accommodate the large number of grids—approximately 2.2 million. As the cross-flow recuperator designs were conventional, the temperature distributions for both recuperators had typical temperature profiles for the cross-flow heat exchanger. The pressure decrease in preheated air was greater than that of flue gas because

the average density in the preheated air was larger. The predicted total heat transfer rates of SiC and MAS recuperators were approximately 56.74 and 56.72 KW, respectively. The primary parameter for total heat transfer rate in this study was the geometry of structure, and the relative effect of thermal conduction was not apparent. The difference between predicted heat transfer rate using STAR-CD and the analytical rate was only 2–4%, indicating that the predicted heat transfer rate was accurate. The predicted temperature and pressure profiles in the first stage of simulation were used for thermal stress analysis of ceramic plate recuperators as the analytical calculation could not provide such information. The result of CATIA analysis demonstrated the metal shell outside the MAS recuperator had a smaller von Mises stress value than that outside the SiC recuperator. Furthermore, ANSYS analytical results demonstrated that the effect of the temperature field was greater than that of the pressure field. The optimal constraint conditions were also identified from simulations.

REFERENCES

1. C. J. Dziedzic, J. J. Cleveland, and R. L. Newman, Heat Recuperative Apparatus Incorporating a Cellular Ceramic Core, United Status Patent 4083400, 1978.
2. M. G. Jeffrey, J. C. Joseph, and H. K. Kent, A Cross-Flow Ceramic Heat Recuperator for Industrial Heat Recovery, *Proc. Industrial Energy Technology Conf.*, pp. 287–300, 1980.
3. S. B. Young, J. W. Bjerklie, and W. A. York, High Temperature Heat Recovery Systems Using Ceramic Recuperators, *Proc. Industrial Energy Technology Conf.*, pp. 273–278, 1980.
4. R. N. Kleiner, L. E. Coubrough, and L. R. Strasbaugh, Compact Ceramic Recuperator for Industrial Heat Recovery, *Proc. Int. Gas Research Conf.*, pp. 55–65, 1984.
5. M. Coombs, H. Strumrf, and D. Kotchic, A Ceramic Finned-Plate Recuperator for Industrial Application, *Proc. Int. Gas Research Conf.*, pp. 846–854, 1984.
6. C. K. Mario, Advanced Ceramic Heat Exchangers Utilizing HEXOLOYTM SA, Single Phase Silicon Carbide Tubes, *Proc. Int. Gas Research Conf.*, pp. 856–863, 1986.
7. M. E. Ward, M. V. Roode, and R. E. Gildersleeve, A New Ceramic Recuperator Technology for Use on High Temperature Processes with Environments Containing Corrosive Agents, *AIChE Symposium Series*, vol. 83, no. 257, pp. 264–271, 1987.
8. C. Ranganayakulu, K. N. Seetharamu, and K. V. Sreevatsan, The Effects of Inlet Fluid Flow Nonuniformity on Thermal Performance and Pressure Drops in Cross-flow Plate-Fin Compact Heat Exchangers, *Inter. J. Heat Mass Transfer*, vol. 40, no. 1, pp. 27–38, 1997.
9. C. Ranganayakulu and K. N. Seetharamu, The Combined Effects of Wall Longitudinal Heat Conduction, Inlet Fluid Flow Nonuniformity and Temperature Nonuniformity in Compact Tube-Fin Heat Exchangers, *Inter. J. Heat and Mass Transfer*, vol. 42, pp. 263–273, 1999.
10. R. T. Ogulata, F. Doba, and T. Yilmaz, Second-Law and Experimental Analysis of a Cross-Flow Heat Exchanger, *Heat Transfer Eng.*, vol. 20, no. 2, pp. 20–27, 1999.
11. D. Bourisa, E. Konstantinidisa, S. Balabanib, D. Castigliab, and G. Bergeles, Design of a Novel-Intensified Heat Exchanger for Reduced Fouling Rates, *Inter. J. Heat and Mass Transfer*, vol. 48, no. 18, pp. 3817–3832, 2005.
12. M. H. Shojaefard, A. R. Noorpoor, D. A. Bozchaloe, and M. Ghaffarpour, Transient Thermal Analysis of Engine Exhaust Valve, *Numer. Heat Transfer A*, vol. 48, no. 7, pp. 627–644, 2005.

13. I. Demirdzic, E. Dzaferovic, and A. Ivankovic, Finite-Volume Approach to Thermo-viscoelasticity, *Numer. Heat Transfer B*, vol. 47, no. 3, pp. 213–237, 2005.
14. N. Tsuzuki, Y. Katoa, and T. Ishiduka, High Performance Printed Circuit Heat Exchanger, *Applied Thermal Eng.*, vol. 27, no. 10, pp. 1702–1707, 2007.
15. B. Yoo, R. F. Kulak, and Y. J. Kim, Pressure and Thermal Stress Analyses of a Generation IV Reactor System Mini-Channel Heat Exchanger, ICONE14, Miami, Florida, USA, 2006.
16. STAR-CD User Manual, Version 3.15 Manual, Computational Dynamics LTD, London, 2001.
17. STAR-CD Methodology Manual, Computational Dynamics LTD, London, 2001.
18. D. P. Dewitt, *Fundamentals of Heat and Mass Transfer*, 4th ed., pp. 69–71. John Wiley & Sons Ltd., New York, 1996.